Anisotropic metamagnetism and magnetotransport of heavy rare-earth orthorhombic single-crystal TbAlGe

Ram Kumar,[1,*] K. E. Avers,[1] V. Saini,[2] D. S. Sokratov,[1] Y. Anand,[1] P. Saraf,[1] J. A. Horn,[1] N. Brenowitz,[1] S. Otazo,[1] P. Sobel,[1] D. Graf,[3] S. R. Saha,[1] and J. Paglione[1,4,†]

[1]*Maryland Quantum Materials Center, Department of Physics, University of Maryland, College Park, Maryland 20742, USA*

[2]*National High Magnetic Field Laboratory, MS E536, Los Alamos National Laboratory, Los Alamos, New Mexico 87545, USA*

[3]*National High Magnetic Field Laboratory, Tallahassee, Florida 32310, USA*

[4]*Canadian Institute for Advanced Research, Toronto, Ontario, Canada M5G 1Z8*

(Received 9 January 2026; revised 31 March 2026; accepted 27 April 2026; published 18 May 2026)

We report a comprehensive investigation of the anisotropic magnetism and magnetic field-induced transitions in single crystals of the orthorhombic system TbAlGe, a member of the topological *R*AlGe (where *R* denotes rare earth) family with the highest ordering temeprature in the *R*Al*X* (X = Si,Ge) series. With a single rare-earth site with triangular coordination in its *Cmcm* orthorhombic unit cell, TbAlGe harbors complex magnetic interactions that yield two antiferromagnetic transitions at 40 and 8 K in zero field, and a rich cascade of metamagnetic transitions that only appear for fields directed along the crystallographic *a*-axis. Combining electrical resistivity, magnetization, and heat capacity measurements with magnetotransport experiments performed up to 41.5 T, we construct a magnetic phase diagram mapping the multiple magnetic phases of TbAlGe, and we discuss the complex interplay between localized $4f$ magnetism and itinerant electronic topology, establishing TbAlGe as a compelling platform for exploring tunable magnetic semimetal physics.

DOI: 10.1103/z39k-8vrq

I. INTRODUCTION

Weyl semimetals exhibit a variety of remarkable physical properties, including topologically protected electronic states that coexist with conventional metallic conduction, giving rise to unconventional transport phenomena. Recently, magnetic topological materials in the family of strongly correlated f-electrons intermetallics have attracted much attention as they provide rich physical properties due to the interplay between correlated-electron phenomena and topological electronic bands [1], which make them valuable for both fundamental research and technological applications [2,3]. More recently, the rare-earth based *R*AlGe (where *R* denotes rare earth) intermetallics have attracted considerable attention as potential Weyl semimetal candidates. This family can host either type I or type II Weyl fermions by breaking time-reversal symmetry or inversion symmetry, or both simultaneously, depending on a suitable choice of the rare-earth species [4–9]. Interestingly, this series can crystallize in both the tetragonal α-$ThSi_2$ type structure for light rare earths, and the orthorhombic YAlGe-type structure for heavy rare earths with space group *Cmcm* [8,10,11]. Although the structures appear different at first glance, they both have the same motif of the "*R*" being enclosed by a triangular prism. The structure with α-$ThSi_2$ type has a triangular prism with $[R_6]$ as the vertices, and the YAlGe type is a triangular prism with $[R_2Al_4]$ as the vertices. With a similar triangular prism, the main feature of the YAlGe-type structure is that the *R* ions form a buckled triangular lattice in the *a*-*c* plane, which may lead to anisotropic exchange interactions in the system.

A majority of the *R*AlGe family exhibits unique magnetic and transport characteristics, often linked to their novel electronic and magnetic structures. *R*AlGe (R = Ce and Pr) show interesting magnetic and electric properties [7,12–19]. The physical properties of single-crystalline NdAlGe show a field-induced metamagnetic transition [20], a large anomalous Hall effect, and helical magnetic structure [21,22]. GdAlGe is found to have two structures, i.e., a high-temperature (HT) phase with tetragonal LaPtSi type ($I4_1md$) and a low-temperature (LT) phase with orthorhombic YAlGe type (*Cmcm*) [10,11,23]. Less attention has been given to the heavy rare-earth systems; to the best of our knowledge, the other heavy rare-earth *R*AlGe intermetallics have only been investigated in their polycrystalline form [10,11,24]. GdAlGe and TbAlGe are only two single-crystal studies of the heavy rare-earth side. Orthorhombic GdAlGe, which is at the transition point between tetragonal and orthorhombic phases in the rare-earth series, has been shown to have Dirac-like linear band dispersion [25]. On the other hand, in TbAlGe, the preliminary polycrystalline study reports an antiferromagnetic (AFM) transition below 40 K [24], while magnetization has only been measured in a single crystal only up to 7 T [26].

In this study, we present a comprehensive investigation of the magnetotransport properties of single crystalline orthorhombic TbAlGe up to magnetic fields as high as 41.5 T. Using magnetotransport, magnetization, and heat capacity measurements performed on single crystals, we characterize the evolution of two AFM states that transition at $T_{N1} = 40$ K

*Contact author: ramphy21@umd.edu
†Contact author: paglione@umd.edu

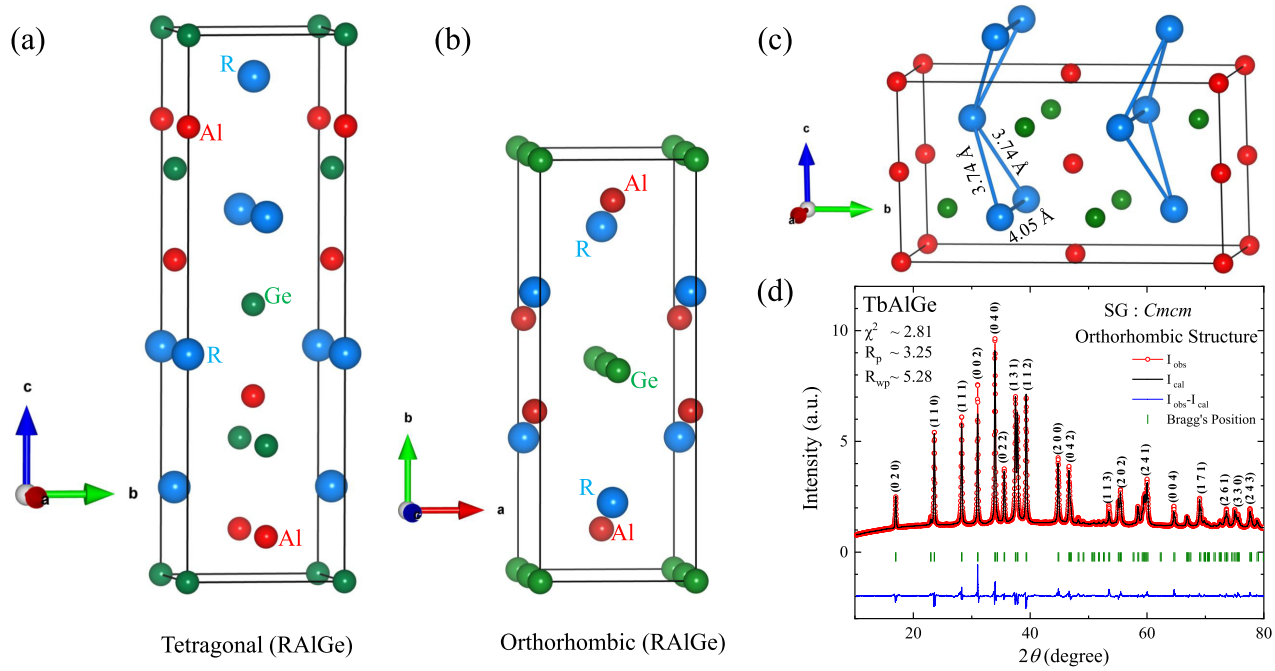

FIG. 1. A comparison of two types of crystal structure of RAlGe, tetragonal (a), and orthorhombic (b). Panel (c) shows the crystal structure with the distorted triangular arrangements of Tb atoms in the orthorhombic crystal structure. Panel (d) represents Rietveld refinement of powder x-ray diffraction data with the experimental data (red symbols) and the black line representing the calculated data. A set of vertical green bars represents the Bragg peak positions of the orthorhombic (space group: *Cmcm*) structure, and the blue line at the bottom represents the difference between the observed and calculated diffraction patterns.

and $T_{N2} = 8$ K at zero field, as they evolve with temperature and magnetic field to reveal a rich texture of multiple metamagnetic transitions only for fields along the crystallographic *a*-axis. We characterize this anisotropic response and discuss how the anisotropic magnetic exchange interactions play a central role in stabilizing the complex spin structures and the tunable landscape for interesting physics in this system.

II. EXPERIMENTAL DETAILS AND CRYSTAL CHEMISTRY

Single crystals of TbAlGe were grown using the high-temperature self-flux technique with molten Al as a solvent. Tb with 99.9% purity, and Al (shot) and Ge (lump) with purity greater than 99.999%, were obtained from Alfa-Aesar. The reactions were carried out in 2-cm^3 alumina crucibles, which were encapsulated in evacuated fused silica jackets by flame sealing. The temperature profile was as follows: ramping to 1100 °C at a rate of 100 °C/h, homogenization for up to 24 h, cooling to 850 °C at a rate of 2 °C/h. At 850 °C, the molten Al was removed by centrifugation. The as-grown crystal is shown in the inset of Fig. 1(b). The phase purity of these crystals was checked with an x-ray diffractometer (Rigaku, MiniFlex600), where x-ray diffraction (XRD) patterns were recorded with monochromated Cu-$K\alpha$ radiation ($\lambda \sim 1.5406$ Å), and crystal orientation along principal crystallographic directions was determined by Laue diffraction using a polychromatic x-ray source. The Rietveld refinement technique [27] using FullProf software packages has been used for phase identification. Further, the chemical composition is verified using a scanning electron microscope (SEM) with an energy-dispersive x-ray spectroscopy (EDS). The magnetic measurements were carried out using a SQUID-VSM, Quantum Design, and Dynacool with VSM-mode for a magnetic field ($B = \mu_0$H) up to 14 T. For every magnetic measurement, the magnetic field was oscillated to zero before each measurement to minimize residual magnetic flux trapped in the superconducting solenoid. Thermodynamic and electrical transport measurements were performed in the range 1.8–300 K and up to 14 T using a Dynacool cryostat (Quantum Design). High-field magneto-transport measurements were performed using a single-axis rotation probe in a 41.5 T resistive magnet (Cell-6) at the National High Magnetic Field Laboratory, with a base temperature of ~1.5 K provided by a variable temperature insert.

III. RESULTS AND DISCUSSION

A. Structural properties

Figure 1(a) shows the crystal structure of TbAlGe, which clearly depicts the triangular lattice of Tb-atoms with opposite slanting to the nearest triangular lattice, and Fig. 1(b) shows the Rietveld refinement of the powder XRD data obtained after grinding the single crystals at room temperature. Structural analysis confirms that our TbAlGe crystals are in the orthorhombic structural phase, and not the tetragonal phase shown by the lighter rare-earth compounds of the RAlGe series [28]. Detailed powder XRD refinements converge in the space group *Cmcm* with *a*- *b*- and *c*-axis lattice parameters 4.045(1), 10.439(1), and 5.767(1) Å, respectively, which correspond well to previous polycrystalline studies [24]. EDS performed on the cleaned surfaces of the single crystal yielded an atomic composition of 31.66(2)% Tb, 32.02(1)% Al, and

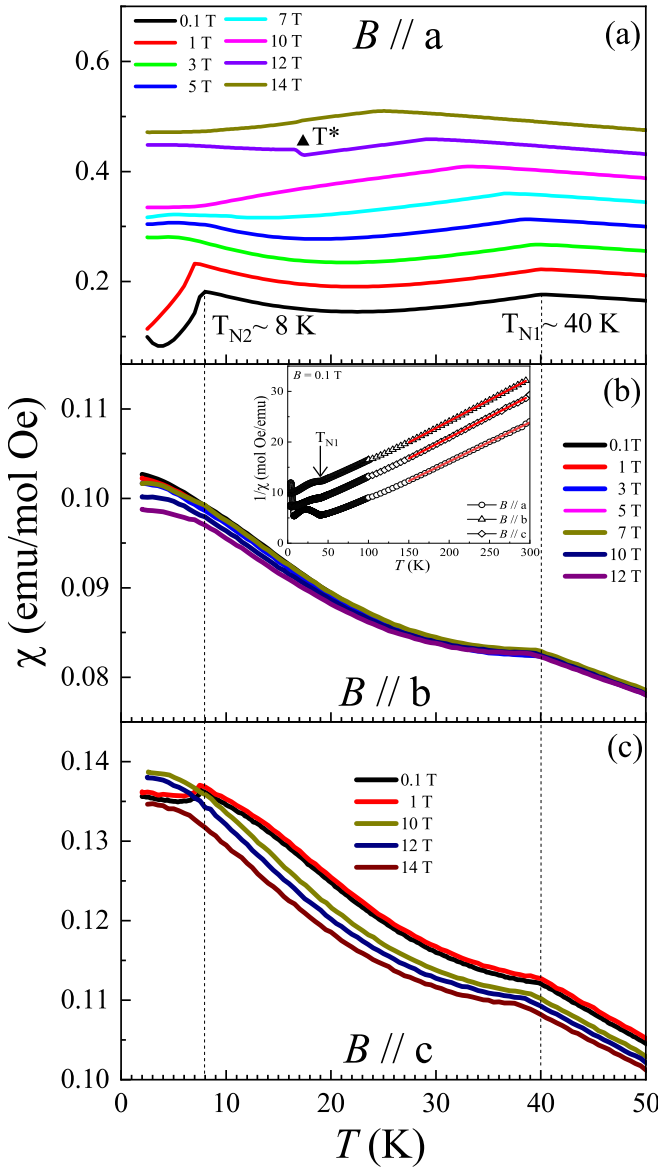

FIG. 2. Temperature dependence of magnetic susceptibility $\chi_{dc}(T)$ of TbAlGe measured under a magnetic field from 0.1 to 14 T in all three $B \parallel a$, $B \parallel b$, and $B \parallel c$ directions as shown in (a), (b), and (c), respectively. The vertical dotted lines across all three panels mark the existing magnetic transitions at $B = 0.1$ T. The curves in (a) are shifted upward for clarity to illustrate the magnetic transition under applied fields. A black triangle symbol is showing a field-induced transition (T^*). The inset of (b) shows the Curie-Weiss fit. All data are measured on warming after cooling in a zero field.

36.32(1)% Ge for TbAlGe. These values are in good agreement with the compositions obtained from XRD refinement.

B. Magnetic properties

Figure 2 presents the temperature-dependent dc-magnetic susceptibility $\chi_{dc}(T)$ of TbAlGe measured in the zero-field-cooled mode with different applied fields along the three principal crystallographic axes. It is observed that $\chi_{dc}(T)$ exhibits two AFM phase transitions at the Néel temperatures of $T_{N1}\sim$ 40 K and $T_{N2}\sim$ 8 K. The Curie-Weiss temperatures and

TABLE I. Curie-Weiss fitting parameters obtained from inverse magnetic susceptibility in the paramagnetic region for different field orientations.

Field direction	μ_{eff} (μ_B/Tb)	θ_P (K)
$B \parallel a$	10.19	−9.5
$B \parallel b$	9.78	−88.1
$B \parallel c$	9.86	−53.7

the effective magnetic moment of the Tb ions are estimated by fitting the inverse susceptibility $(1/\chi)$ with the modified Curie-Weiss law, $\chi(T) = \chi_0 + C/(T-\theta_P)$, in the paramagnetic region 150–300 K, as shown in the inset of Fig. 2(b). Here, χ_0, C, and θ_P are the temperature-independent susceptibility, Curie constant, and paramagnetic Curie-Weiss temperature, respectively. The Curie-Weiss fits of inverse susceptibilities in the paramagnetic (PM) region for magnetic fields parallel to all three principal axes are shown in Table I. The effective magnetic moment determined experimentally is comparable to the theoretical free-ion value of $9.72\mu_B$ for the Tb^{3+} ion. The negative θ_P indicates that antiferromagnetic exchange interactions dominate in the system. The difference in the calculated values of θ_P along different magnetic field directions, particularly along the field parallel to the a-axis, infers the role of strong magnetic anisotropy/single-ion anisotropy of Tb [29,30], due to different magnetic-site interactions present in the system. Next, to gain a deeper insight into the behavior of these anisotropic magnetic phase transitions, we have measured $\chi_{dc}(T)$ with different applied magnetic fields up to 14 T in all three directions. The $\chi_{dc}(T)$ plots with applied magnetic fields for $B \parallel a$ look distinctive, as shown in Fig. 2(a). With increasing magnetic field, T_{N2} is rapidly suppressed and disappears above ∼5 T. In contrast, the higher-temperature transition T_{N1} gradually shifts to lower temperatures with increasing field, reaching ∼24 K at 14 T. In addition, a new field-induced feature emerges, as observed in the 12 T susceptibility shown in Fig. 2(a). This transition, labeled T^*, is distinct from T_{N2} and is only observed for $B \parallel a$. The field dependence of this phase transition is discussed in Fig. 8. There is not much variation in T_{N1} and T_{N2} for the cases $B \parallel b$ and $B \parallel c$ [Figs. 2(b) and 2(c)]. Additionally, the distorted triangular lattice of Tb may promote anisotropic magnetic interactions, contributing to the emergence of these intriguing magnetic phases. Note that the Néel temperature of TbAlGe (T_{N1} = 40 K) is markedly higher than the value of ∼20 K expected from de Gennes scaling based on the Gd analog (T_N = 30 K) [25]. This enhancement indicates a breakdown of simple RKKY scaling, likely caused by strong anisotropic exchange interactions and crystal-field effects [31]. Such behavior underscores the complex interplay between localized $4f$ magnetism and itinerant electron topology in such a magnetic system. To further investigate the effect of the magnetic field, we have measured isothermal magnetization at selected temperatures up to 50 K. Figure 3(a) shows magnetization as a function of the field at different temperatures between 2 and 35 K for $B \parallel a$. An interesting observation is that, at the lowest measured temperature (2 K), significant hysteresis is observed on the slopes of the $M(B)$ curves near 3 and 11 T. Such a

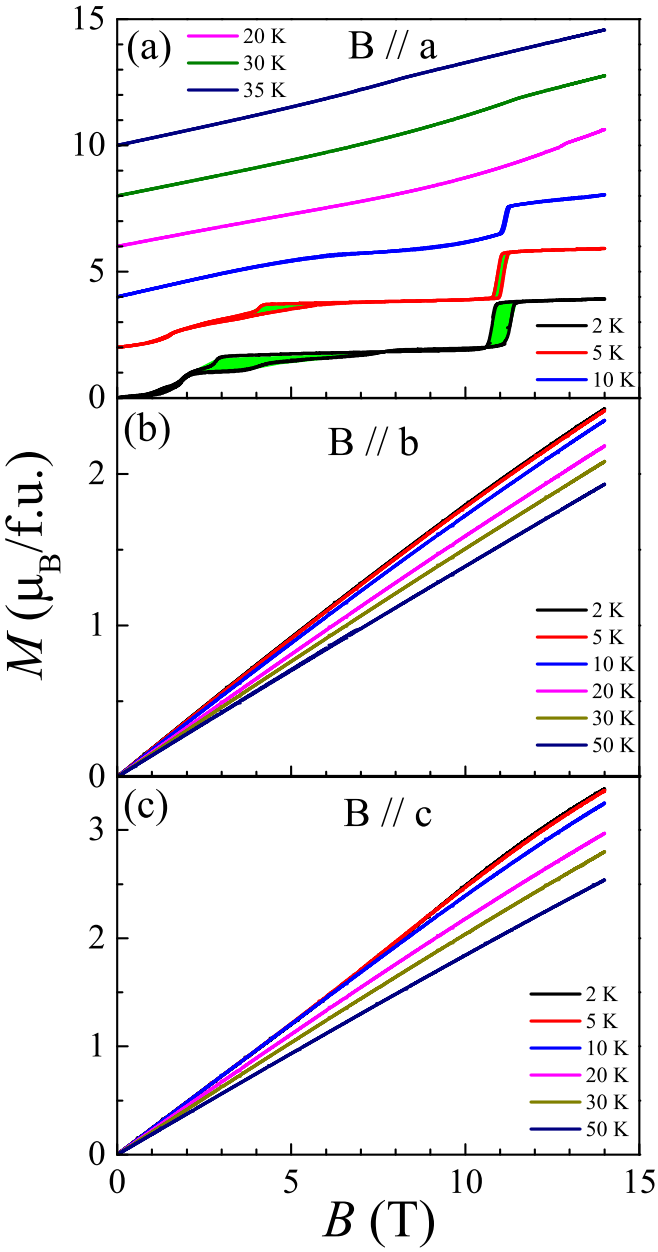

FIG. 3. Magnetic field (B) dependence of magnetization (M) of TbAlGe measured at different temperatures for the applied magnetic field parallel to three principal crystallographic directions, i.e., (a) $B \parallel a$, (b) $B \parallel b$, and (c) $B \parallel c$, respectively. We note that for $B \parallel a$, there are multiple metamagnetic transitions, while the other field directions are mostly featureless with minor curvature. The curves in (a) are shifted upward for clarity to illustrate the hysteresis at each metamagnetic transition.

first-order-like magnetic transition gradually gets smeared with increasing temperature. The transition observed around 11 T shifts to higher fields with increasing temperature, suggesting the presence of more intriguing magnetic behavior at further higher field values. The $M(B)$ curves for other directions are observed to be predominantly reversible with magnetic field directions without any field-induced transition. Moreover, $M(B)$ curves do not saturate even in a 14 T field at 2 K, and the spontaneous magnetic moment at 2 K is only $4\mu_B/\mathrm{Tb}^{3+}$ (even lower for other directions), which is less than half of the free Tb^{3+} magnetic moment. A comprehensive determination of the magnetic structure is necessary to clarify this behavior. Detailed inelastic neutron scattering experiments are necessary to directly elucidate the role of anisotropic exchange interactions in the observed anisotropic metamagnetic transitions. The suggested change in the magnetic structure at the lower transition temperature is further supported by the first-order magnetic phase transition observed near 8 K in TbAlGe, which may be associated with a change in the magnetic propagation vector driven by anisotropic exchange interactions. Moreover, the crystal structure reveals an isosceles triangular arrangement of Tb atoms along the a-axis, perpendicular to the ($0kl$) planes. This geometrical motif likely underpins the unusual metamagnetic behavior observed exclusively for magnetic fields applied along the a-axis ($B \parallel a$).

C. Heat capacity and magnetocaloric effect

We report the results of zero-field and in-field heat capacity, $C_P(T)$, measurements of TbAlGe as a function of temperature, which is shown in Fig. 4(a). There is a well-defined λ anomaly at $T_{N1}\sim$ 40 K and another magnetic transition at a much lower temperature, $T_{N2}\sim$ 8 K, which is also seen in the magnetic measurements. Both peaks at T_{N1} and T_{N2} are gradually shifted towards lower temperatures with an increase in applied magnetic fields below 5 T. For $B = 5$ T (blue solid line), the T_{N2} is smeared out, which shows how delicate the transition is compared to T_{N1}, despite both being antiferromagnetic-type transitions. Such an interesting behavior might be due to a modulated AFM structure, which needs to be further investigated by neutron scattering. As calculated from the linear fitting of the low-temperature $C_P/T(T^2)$ data of TbAlGe [as shown in the insets of Fig. 4(a)], the Sommerfeld coefficient, $\gamma =$ 88 mJ/mol K^2, suggests strong electronic correlations. The lower panels of Fig. 4 show the C_P/T as a function of temperature, providing a clearer view of the effects of the applied magnetic field on these magnetic phase transitions in TbAlGe.

We have studied the magnetocaloric effect (MCE) or magnetic entropy change, $-\Delta S_M$ (the change induced in the entropy, S, by the application of B at a given T), in TbAlGe, particularly along the a-axis, which seems to be a peculiar one compared to other principal axes, to get more information about the different magnetic phase transitions, as studied in other Tb compounds [32–38]. We have measured many isothermal $M(B)$ curves for different temperatures with close intervals of 2 up to 50 K to calculate the MCE. These values have been derived for an initial B of zero and final B marked in the figures. The ΔS from M data is determined through the Maxwell relation, $[\partial \mathrm{S}(T,B)/\partial \mathrm{H}]_T = [\partial \mathrm{M}(T,B)/\partial \mathrm{T}]_B$ [39]. We have derived the isothermal entropy change, defined as $-\Delta S_M$, up to 50 K, and the result obtained is shown in Fig. 5. The magnetic susceptibility data corroborate well with the two magnetic phase transitions revealed from magnetic entropy as well. In addition, the sign of $-\Delta S_M$ is flipped twice below the magnetic ordering: (i) around 20 K, exactly where χ shows a minima between the two transitions [Fig. 2(a)], which indicates the strong competition among

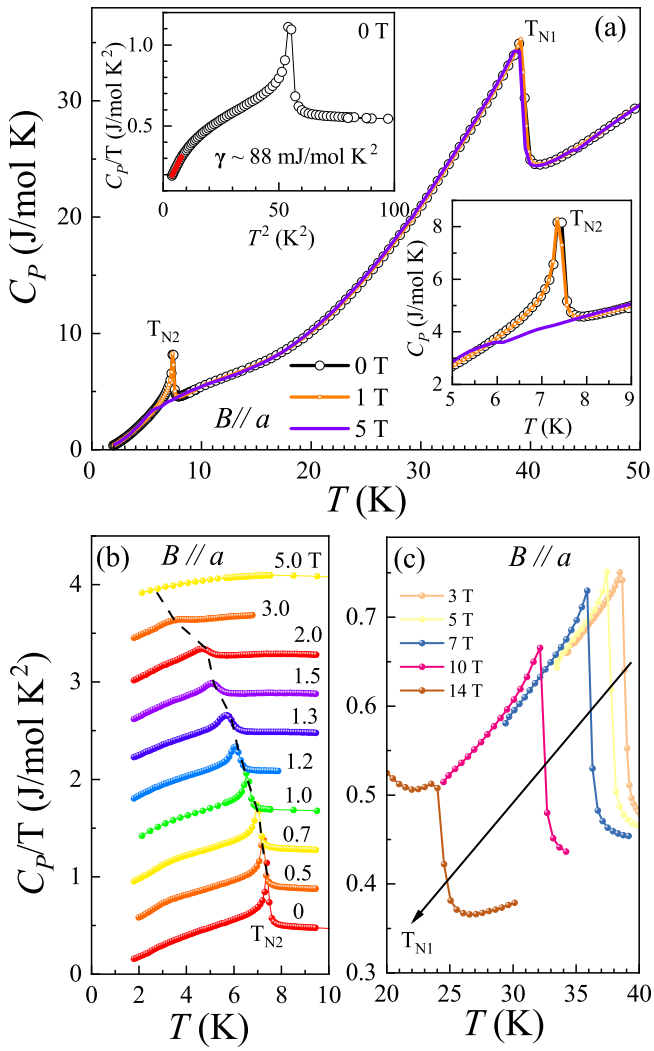

FIG. 4. (a) Temperature dependence of heat capacity of TbAlGe measured under zero field and applied magnetic fields. The upper left inset shows the C_P/T vs T^2 plot in zero field with the red solid line at the low-temperature region showing the linear fit to calculate the γ. The bottom right inset shows the suppression of T_{N2} with an increase in the applied magnetic field. The C_P/T vs T plots with different applied magnetic fields for a better view of T_{N1} and T_{N2} are shown in (b) and (c), respectively.

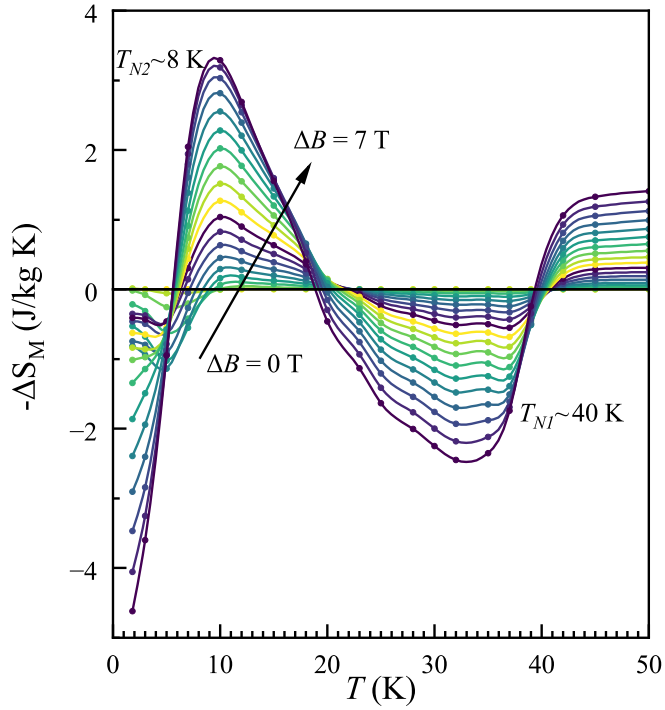

FIG. 5. Change in magnetic entropy ($-\Delta S$) of TbAlGe as a function of temperature at different magnetic fields from 0 to 7 T in 0.025 T steps. The observed sign change in entropy reveals possible competing magnetic phases that evolve with temperature and magnetic field.

the magnetic interactions and implies the dominance of an antiferromagnetic component over the ferromagnetic (FM) phase [40], and (ii) at low temperature just below T_{N2}, where we expect a possible first-order magnetic phase transition (also discussed in magnetization); at higher temperatures, the sign of $-\Delta S_M$ is positive, which is a signature of a tendency for spin-reorientation [41], suggesting the dominance of ferromagnetic correlations in the presence of such magnitudes of external fields. The presence of a possible first-order magnetic transition below 8 K, manifested through magnetic hysteresis (Fig. 3) and corroborated by magnetotransport data (Figs. 6 and 7), together with multiple sign reversals of the magnetic entropy, points to the significant magnetocaloric potential in this compound.

D. Magnetotransport properties up to a high magnetic field of 41.5 T

We have measured detailed zero-field and in-field transverse electrical resistivity ρ as a function of temperature in both the $B \parallel a$ and $B \parallel b$ directions, as shown in Figs. 6(a) and 6(b), respectively. The residual resistivity ratio (RRR), calculated as $\rho(300\,\mathrm{K})/\rho(1.8\ \mathrm{K})$ and equal to about 13 [as shown in the inset of (b)], indicates fair crystal quality. The electrical resistivity of TbAlGe shows metallic behavior, but exhibits an anomaly as the system approaches T_{N1} from higher temperatures. Below T_{N1}, the loss of spin-disorder scattering due to long-range AFM ordering leads to a rapid decrease in resistivity. There is a clear, sharp drop in ρ at T_{N1} in the zero-field resistivity data, Figs. 6(a) and 6(b). With further lowering of the temperature, there is a shoulder/humplike feature near 8 K as the system enters another magnetic phase. These anomalies at the onset of magnetic ordering manifest differently depending on the magnetic field direction along different crystallographic directions. Similar to the magnetic susceptibility shown in Fig. 2(a), T^* is also observed in the resistivity only for $B \parallel a$. To further explore the existing magnetic phases at higher fields, we have measured the magnetoresistance (MR) at several temperatures for $B \parallel a$ and $B \parallel b$ as shown in Figs. 6(c) and 6(d), respectively. Having multiple metamagnetic transitions along the a-axis, similar to magnetization, confirms that $B \parallel a$ is the most favorable direction for observing emergent magnetotransport properties.

The novel features observed in the magnetic and magnetotransport measurements motivate us to study higher magnetic fields (B = 41.5 T), mainly for the applied magnetic field

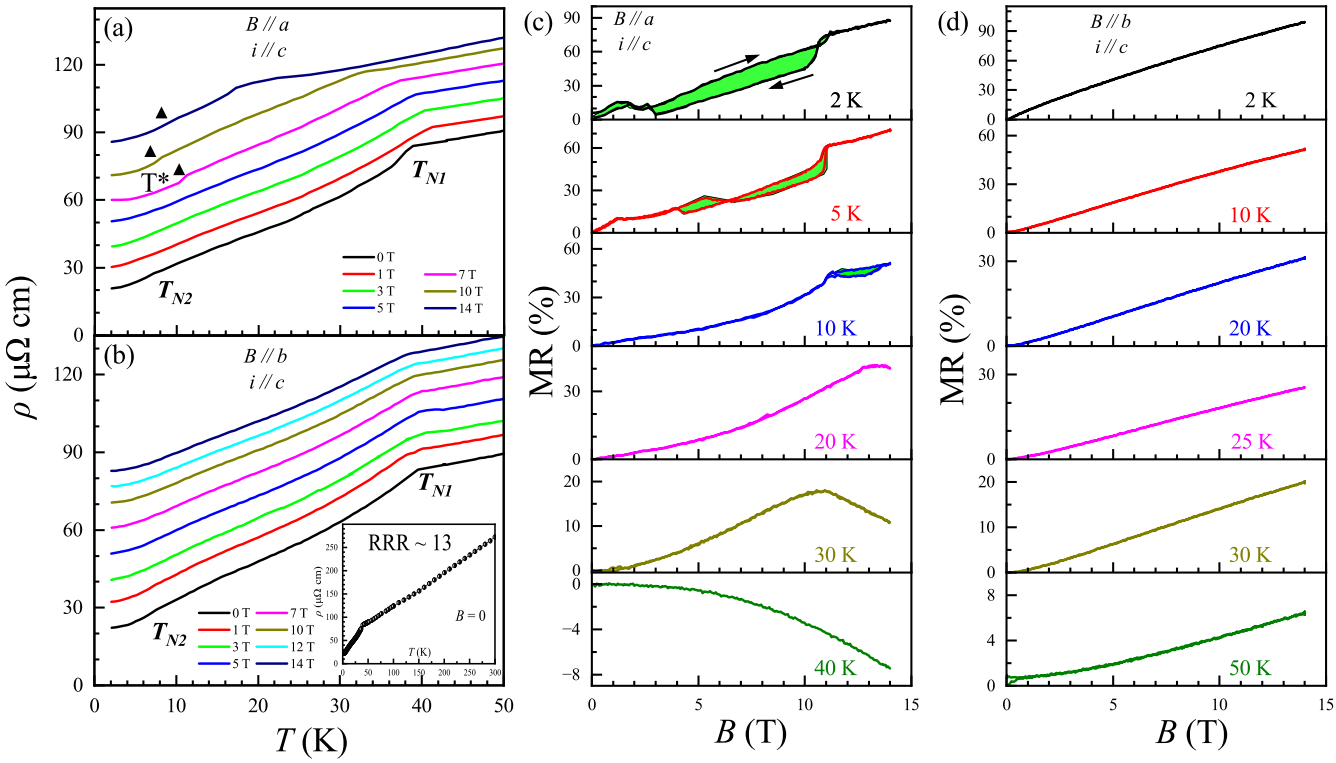

FIG. 6. Electrical resistivity (ρ) as a function of the temperature under different applied fields. (a) $\rho_{xx}(T)$ of TbAlGe for $B \parallel a$ and $B \parallel b$ is shown in panels (a) and (b), respectively. The curves above the zero field one are constantly shifted upwards with a factor of 10 $\mu\Omega$ cm for the clarity of the magnetic transition under applied fields. Black triangles in (a) show the field-induced transition (T^*). The inset of (b) shows the $\rho_{xx}(T)$ up to 300 K. The transverse magnetoresistance of TbAlGe and its evolution with temperature for $B \parallel a$ and $B \parallel b$ are shown in (c) and (d), respectively.

along the a-axis. The MR behavior at different temperatures starting from base temperature, $T = 1.5$ to 35 K (in the magnetic state), is shown in Fig. 7. The symmetrized magnetoresistance data to remove the contribution from the Hall component using $\mathrm{MR}(B) = [\mathrm{MR}(B) + \mathrm{MR}(-B)]/2$ are shown here. The curves for temperatures above 1.5 K are constantly shifted upward (with a factor of 60%) for clarity to illustrate the multiple field-induced transitions. Interestingly, a clear hysteresis is observed between the up-sweep and down-sweep magnetoresistance curves, but only below 10 K. This hysteretic behavior, consistent with that seen in magnetization, further reinforces the presence of a first-order magnetic phase transition in TbAlGe. Measurements in magnetic fields up to 41.5 T show an additional set of metamagnetic transitions beyond those detected in the PPMS measurements up to 14 T. These metamagnetic transitions are labeled sequentially from 1 to 5; for instance, the first metamagnetic transition is denoted as MMT1 (as plotted along with the contour plot in Fig. 8). In particular, the magnetoresistance reaches approximately 120% at 1.5 K around 18 T. Notably, TbAlGe hosts both first-order and second-order magnetic phase transitions, consistent with the rich field-induced phase diagram (which will be discussed in the next section).

E. Phase diagram

Our results can be summarized in the magnetic phase diagram of TbAlGe, measured down to 1.5 K and up to an applied magnetic field of 41.5 T. Contour plots of magnetoresistance ($B = 0$–41.5 T) are shown in Fig. 8, where the white data points mark the transition temperatures T_{N1}, T_{N2}, and T^*, determined from the derivative of the magnetic susceptibility. The high-field magnetoresistance data presented in Fig. 7 are used to identify a series of metamagnetic transitions (MMTs) and to construct the phase diagram. At 1.5 K, five distinct metamagnetic transitions are observed in the range of 2–26 T, labeled as MMT1 through MMT5, separating multiple magnetic phases (MP-1 to MP-5). Among these, MMT2 exhibits two distinct shoulders (2^u and 2^d) at different magnetic fields of up- and down-sweep in MR traces, indicating a first-order transition. In contrast, the remaining transitions show no such crossing; however, significant hysteresis is observed from the touching points of the up- and down-sweep MR curves. The shoulders in the up-sweep MR curves are used to further determine the phase boundaries of all the MMTs. With increasing temperature, the hysteresis associated with these MMTs becomes progressively narrower, as observed in Fig. 7, suggesting a weakening of the first-order character. The resulting phase diagram consists of multiple magnetic phases separated by these transitions. The first antiferromagnetic (AFM) phase eventually merges with the fifth magnetic phase (MP-5) around 26 T, clearly delineating the boundary between the field-polarized (FP) phase and the lower-field phases. The phase diagram highlights the fragility of the magnetic phases between the two antiferromagnetic transitions (T_{N1} and T_{N2}), along with an additional field-induced transition (T^*), revealing a complex interplay of competing magnetic

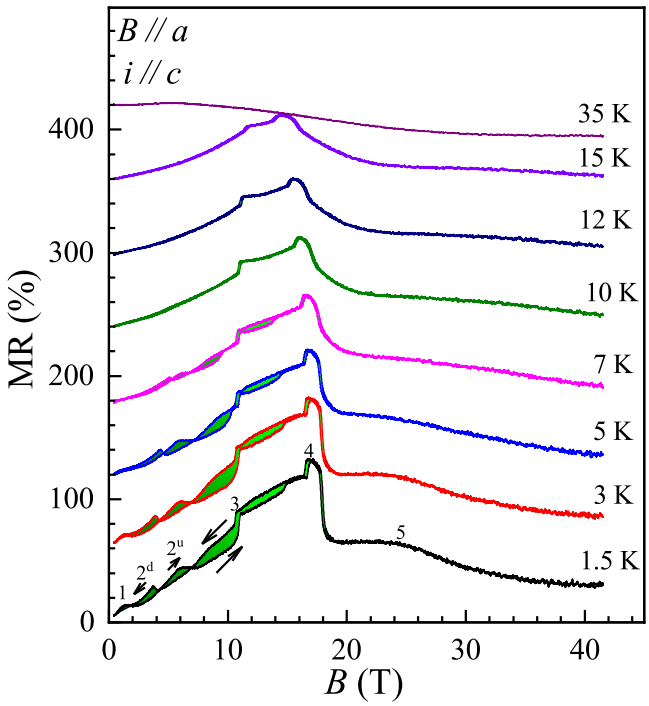

FIG. 7. High-field magnetoresistance as a function of the magnetic field at different temperatures in the magnetic state for $B \parallel a$. The curves for temperatures above 1.5 K are constantly shifted upward (with a factor of 60%) for clarity to illustrate the multiple field-induced transitions as marked with different number (where "u" denotes up sweep and "d" denotes down sweep) symbols for 1.5 K curve.

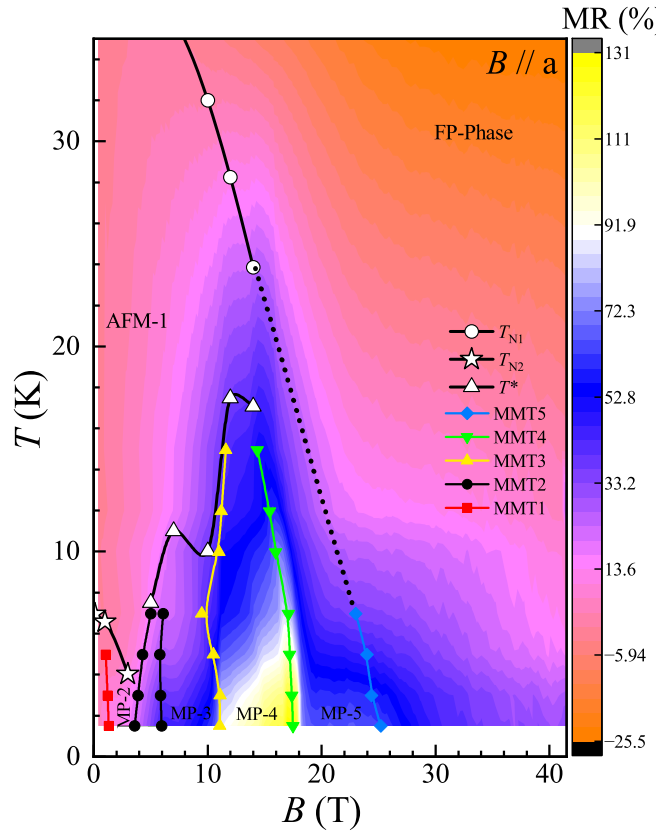

FIG. 8. *B-T* phase diagram of TbAlGe as a contour plot of magnetoresistance up to 41.5 T, with T_{N1}, T_{N2}, and T^* obtained from magnetic susceptibility measurements. The different metamagnetic transitions are derived from the magnetoresistance plot as shown in Fig. 7.

interactions. There is strong agreement between transport and magnetic measurements, particularly in the overlapping temperature range. These phase transitions are also reflected in the magnetic entropy, where sign changes correspond to different magnetic phases. The sliding triangular arrangement of Tb atoms with distorted bond lengths may introduce moderate geometrical frustration. The presence of anisotropic exchange interaction due to frustration gives rise to the possibility of exotic magnetism, as seen in other geometrically frustrated heavy rare-earth magnets as well [29,33,34,42–46]. The resulting anisotropic exchange interactions likely play a key role in stabilizing the nontrivial spin structures in TbAlGe, which may host topological electronic states.

IV. CONCLUSION

In conclusion, we have grown single crystals of the heavy rare-earth system TbAlGe and performed detailed magnetic and magnetotransport studies on this metallic antiferromagnet, which crystallizes in the orthorhombic *Cmcm* structure. TbAlGe exhibits two antiferromagnetic transitions at $T_{N1} = 40$ K and $T_{N2} = 8$ K, developing a rich, field-tuned magnetic phase diagram with multiple metamagnetic transitions at 1.5 K. Notably, unlike other heavy rare-earth RAlGe compounds, TbAlGe displays a strongly first-order transition near 6 T in the vicinity of the lower Néel temperature. High-field measurements up to 41.5 T reveal additional metamagnetic transitions beyond those observed in conventional measurements up to 14 T, highlighting sophisticated anisotropic magnetic interactions, likely influenced by the distorted triangular lattice of terbium. These results provide key insights into the interplay between magnetism and Fermi-surface topology in TbAlGe, making it an ideal platform to study correlated electronic physics. Future studies combining band-structure calculations and neutron scattering experiments will be essential to fully elucidate the connection between the magnetic phases and the topological electronic structure in this system.

ACKNOWLEDGMENTS

Research at the University of Maryland was supported by the Gordon and Betty Moore Foundation's EPiQS Initiative through Grant No. GBMF9071, the US National Science Foundation (NSF) Grant No. DMR2303090, the Binational Science Foundation Grant No. 2022126, and the Maryland Quantum Materials Center. R.K. acknowledges support from the NSF Grant No. 2201516 under the Accelnet program of Office of International Science and Engineering (OISE). A portion of this work was performed at the National High Magnetic Field Laboratory, which is supported by National Science Foundation Cooperative Agreement No. DMR-2128556 and the State of Florida. S.R.S. acknowledges support from the National Institute of Standards and Technology Cooperative Agreement No. 70NANB17H301.

DATA AVAILABILITY

The data that support the findings of this article are not publicly available upon publication because it is not technically feasible and/or the cost of preparing, depositing, and hosting the data would be prohibitive within the terms of this research project. The data are available from the authors upon reasonable request.

[1] B. A. Bernevig, C. Felser, and H. Beidenkopf, Progress and prospects in magnetic topological materials, Nature (London) **603**, 41 (2022).

[2] K. H. J. Buschow, Intermetallic compounds of rare-earth and 3d transition metals, Rep. Prog. Phys. **40**, 1179 (1977).

[3] C. Pfleiderer, Superconducting phases of f-electron compounds, Rev. Mod. Phys. **81**, 1551 (2009).

[4] W. Cao, N. Zhao, C. Pei, Q. Wang, Q. Zhang, T. Ying, Y. Zhao, L. Gao, C. Li, N. Yu, L. Gu, Y. Chen, K. Liu, and Y. Qi, Pressure-induced superconductivity in the noncentrosymmetric Weyl semimetals LaAlX (X = Si, Ge), Phys. Rev. B **105**, 174502 (2022).

[5] H. Su, X. Shi, J. Yuan, Y. Wan, E. Cheng, C. Xi, L. Pi, X. Wang, Z. Zou, N. Yu, W. Zhao, S. Li, and Y. Guo, Multiple Weyl fermions in the noncentrosymmetric semimetal LaAlSi, Phys. Rev. B **103**, 165128 (2021).

[6] S.-Y. Xu, N. Alidoust, G. Chang, H. Lu, B. Singh, I. Belopolski, D. S. Sanchez, X. Zhang, G. Bian, H. Zheng, M.-A. Husanu, Y. Bian, S.-M. Huang, C.-H. Hsu, T.-R. Chang, H.-T. Jeng, A. Bansil, T. Neupert, V. N. Strocov, H. Lin, *et al.*, Discovery of Lorentz-violating type II Weyl fermions in LaAlGe, Sci. Adv. **3**, e1603266 (2017).

[7] H. Hodovanets, C. J. Eckberg, P. Y. Zavalij, H. Kim, W.-C. Lin, M. Zic, D. J. Campbell, J. S. Higgins, and J. Paglione, Single-crystal investigation of the proposed type-II Weyl semimetal CeAlGe, Phys. Rev. B **98**, 245132 (2018).

[8] P. Puphal, V. Pomjakushin, N. Kanazawa, V. Ukleev, D. J. Gawryluk, J. Ma, M. Naamneh, N. C. Plumb, L. Keller, R. Cubitt, E. Pomjakushina, and J. S. White, Topological magnetic phase in the candidate Weyl semimetal CeAlGe, Phys. Rev. Lett. **124**, 017202 (2020).

[9] W. Liu, J. Zhao, F. Meng, A. Rahman, Y. Qin, J. Fan, L. Pi, Z. Tian, H. Du, L. Zhang, and Y. Zhang, Critical behavior of the magnetic Weyl semimetal PrAlGe, Phys. Rev. B **103**, 214401 (2021).

[10] C. Wang, Y. Guo, and T. Wang, Magnetic and transport properties of orthorhombic rare-earth aluminum germanide GdAlGe, J. Magn. Magn. Mater. **526**, 167739 (2021).

[11] C. Wang, Y. Guo, and T. Wang, Dynamic evolution from positive to negative magnetoresistance of RAlGe (R = Dy, Ho) with disordered orthorhombic structure, J. Alloys Compd. **902**, 163623 (2022).

[12] S. Pukas, Y. Lutsyshyn, M. Manyako, and E. Gladyshevskii, Crystal structures of the RAlSi and RAlGe compounds, J. Alloys Compd. **367**, 162 (2004).

[13] H. Flandorfer, D. Kaczorowski, J. Gröbner, P. Rogl, R. Wouters, C. Godart, and A. Kostikas, The systems Ce–Al–(Si, Ge): Phase equilibria and physical properties, J. Solid State Chem. **137**, 191 (1998).

[14] T. Suzuki, L. Savary, J.-P. Liu, J. W. Lynn, L. Balents, and J. G. Checkelsky, Singular angular magnetoresistance in a magnetic nodal semimetal, Science **365**, 377 (2019).

[15] K. Singh and K. Mukherjee, Spin–lattice relaxation phenomena in the magnetic state of a suggested Weyl semimetal CeAlGe, Philos. Mag. **100**, 1771 (2020).

[16] B. Meng, H. Wu, Y. Qiu, C. Wang, Y. Liu, Z. Xia, S. Yuan, H. Chang, and Z. Tian, Large anomalous Hall effect in ferromagnetic Weyl semimetal candidate PrAlGe, APL Mater. **7**, 051110 (2019).

[17] D. Destraz, L. Das, S. S. Tsirkin, Y. Xu, T. Neupert, J. Chang, A. Schilling, A. G. Grushin, J. Kohlbrecher, L. Keller, P. Puphal, E. Pomjakushina, and J. S. White, Magnetism and anomalous transport in the Weyl semimetal PrAlGe: Possible route to axial gauge fields, npj Quantum Mater. **5**, 5 (2020).

[18] D. S. Sanchez, G. Chang, I. Belopolski, H. Lu, J.-X. Yin, N. Alidoust, X. Xu, T. A. Cochran, X. Zhang, Y. Bian, S. S. Zhang, Y.-Y. Liu, J. Ma, G. Bian, H. Lin, S.-Y. Xu, S. Jia, and M. Z. Hasan, Observation of Weyl fermions in a magnetic non-centrosymmetric crystal, Nat. Commun. **11**, 3356 (2020).

[19] H.-Y. Yang, B. Singh, B. Lu, C.-Y. Huang, F. Bahrami, W.-C. Chiu, D. Graf, S.-M. Huang, B. Wang, H. Lin, D. Torchinsky, A. Bansil, and F. Tafti, Transition from intrinsic to extrinsic anomalous Hall effect in the ferromagnetic Weyl semimetal PrAlGe$_{1-x}$Si$_x$, APL Mater. **8**, 011111 (2020).

[20] J. Zhao, W. Liu, A. Rahman, F. Meng, L. Ling, C. Xi, W. Tong, Y. Bai, Z. Tian, Y. Zhong, Y. Hu, L. Pi, L. Zhang, and Y. Zhang, Field-induced tricritical phenomenon and magnetic structures in magnetic Weyl semimetal candidate NdAlGe, New J. Phys. **24**, 013010 (2022).

[21] C. Dhital, R. L. Dally, R. Ruvalcaba, R. Gonzalez-Hernandez, J. Guerrero-Sanchez, H. B. Cao, Q. Zhang, W. Tian, Y. Wu, M. D. Frontzek, S. K. Karna, A. Meads, B. Wilson, R. Chapai, D. Graf, J. Bacsa, R. Jin, and J. F. DiTusa, Multi-k magnetic structure and large anomalous Hall effect in candidate magnetic Weyl semimetal NdAlGe, Phys. Rev. B **107**, 224414 (2023).

[22] H.-Y. Yang, J. Gaudet, R. Verma, S. Baidya, F. Bahrami, X. Yao, C.-Y. Huang, L. DeBeer-Schmitt, A. A. Aczel, G. Xu, H. Lin, A. Bansil, B. Singh, and F. Tafti, Stripe helical magnetism and two regimes of anomalous Hall effect in NdAlGe, Phys. Rev. Mater. **7**, 034202 (2023).

[23] C. Wang, Y.-Q. Guo, T. Wang, and S.-W. Yang, Crystal structure and electromagnetic responses of tetragonal GdAlGe, Chin. Phys. B **29**, 127502 (2020).

[24] C. Wang, Y. Guo, and T. Wang, Correlation between slanted magnetic structure and electromagnetic responses in the RAlGe (R = Tb and Er) system, J. Phys. Chem. C **125**, 21764 (2021).

[25] A. Laha, J. Yao, A. K. Kundu, N. Aryal, A. Rajapitamahuni, E. Vescovo, F. Camino, K. Kisslinger, L. Zhang, D. Nykypanchuk, J. Sears, J. M. Tranquada, W. Yin, and Q. Li, Single-crystalline orthorhombic GdAlGe as a rare-earth magnetic Dirac nodal-line metal, Phys. Rev. B **112**, 125155 (2025).

[26] K. Gouda and T. Nishioka, Angular-field magnetic phase diagram of b-plane at 4 K of YAlGe-type TbAlGe with zigzag-chain, J. Phys.: Conf. Ser. **2164**, 012072 (2022).

[27] H. M. Rietveld, A profile refinement method for nuclear and magnetic structures, J. Appl. Crystallogr. **2**, 65 (1969).

[28] A. M. Guloy and J. D. Corbett, Syntheses and structures of lanthanum germanide, $LaGe_{2-x}$, and lanthanum aluminum germanide, LaAlGe: interrelationships among the α-$ThSi_2$, α-$GdSi_2$, and LaPtSi structure types, Inorg. Chem. **30**, 4789 (1991).

[29] R. Wawrzyńczak, B. Tomasello, P. Manuel, D. Khalyavin, M. D. Le, T. Guidi, A. Cervellino, T. Ziman, M. Boehm, G. J. Nilsen, and T. Fennell, Magnetic order and single-ion anisotropy in $Tb_3Ga_5O_{12}$, Phys. Rev. B **100**, 094442 (2019).

[30] R. Kumar, S. Rayaprol, S. Rajput, T. Maitra, D. T. Adroja, K. K. Iyer, S. K. Upadhyay, and E. V. Sampathkumaran, Existence of a critical canting angle of magnetic moments to induce multiferroicity in the Haldane spin-chain system Tb_2BaNiO_5, Phys. Rev. B **99**, 100406 (2019).

[31] S. Majumdar and E. Sampathkumaran, Multiple magnetic transitions and anomalous magnetism in Tb_2CuGe_3, Solid State Commun. **117**, 645 (2001).

[32] R. Kumar, K. K. Iyer, P. L. Paulose, and E. V. Sampathkumaran, Competing magnetic interactions and magnetoresistance anomalies in cubic intermetallic compounds, Gd_4RhAl and Tb_4RhAl, and enhanced magnetocaloric effect for the Tb case, Phys. Rev. Mater. **5**, 054407 (2021).

[33] R. Kumar, K. K. Iyer, P. L. Paulose, and E. V. Sampathkumaran, Spin-glass features at multiple temperatures and transport anomalies in Tb_4PtAl, J. Appl. Phys. **126**, 123906 (2019).

[34] R. Kumar, K. K. Iyer, P. L. Paulose, and E. V. Sampathkumaran, Magnetic and transport anomalies in R_2RhSi_3(R = Gd, Tb, and Dy) resembling those of the exotic magnetic material Gd_2PdSi_3, Phys. Rev. B **101**, 144440 (2020).

[35] B. Maji, M. K. Ray, K. G. Suresh, and S. Banerjee, Large exchange bias and magnetocaloric effect in $TbMn_2Si_2$, J. Appl. Phys. **116**, 213913 (2014).

[36] W. Tian, A. Kreyssig, J. L. Zarestky, L. Tan, S. Nandi, A. I. Goldman, T. A. Lograsso, D. L. Schlagel, K. A. Gschneidner, V. K. Pecharsky, and R. J. McQueeney, Single-crystal neutron diffraction study of short-range magnetic correlations in Tb_5Ge_4, Phys. Rev. B **80**, 134422 (2009).

[37] C. Fang, G. Li, J. Wang, W. D. Hutchison, Q. Y. Ren, Z. Deng, G. Ma, S. Dou, S. J. Campbell, and Z. Cheng, New insight into magneto-structural phase transitions in layered $TbMn_2Ge_2$-based compounds, Sci. Rep. **7**, 45814 (2017).

[38] C. Ritter, L. Morellon, P. A. Algarabel, C. Magen, and M. R. Ibarra, Magnetic and structural phase diagram of $Tb_5(Si_xGe_{1-x})_4$, Phys. Rev. B **65**, 094405 (2002).

[39] A. M. Tishin and Y. I. Spichkin, *The Magnetocaloric Effect and Its Applications* (CRC Press, Boca Raton, FL, 2016).

[40] V. K. Pecharsky and K. A. Gschneidner, Jr., Magnetocaloric effect and magnetic refrigeration, J. Magn. Magn. Mater. **200**, 44 (1999).

[41] L. Li and M. Yan, Recent progresses in exploring the rare earth based intermetallic compounds for cryogenic magnetic refrigeration, J. Alloys Compd. **823**, 153810 (2020).

[42] K. Kamazawa, D. Louca, R. Morinaga, T. J. Sato, Q. Huang, J. R. D. Copley, and Y. Qiu, Field-induced antiferromagnetism and competition in the metamagnetic state of terbium gallium garnet, Phys. Rev. B **78**, 064412 (2008).

[43] S. Saha, H. Sugawara, T. D. Matsuda, H. Sato, R. C. Mallik, and E. V. Sampathkumaran, Magnetic anisotropy, first-order-like metamagnetic transitions, and large negative magnetoresistance in single-crystal Gd_2PdSi_3, Phys. Rev. B **60**, 12162 (1999).

[44] T. Kurumaji, T. Nakajima, M. Hirschberger, A. Kikkawa, Y. Yamasaki, H. Sagayama, H. Nakao, Y. Taguchi, T.-h. Arima, and Y. Tokura, Skyrmion lattice with a giant topological Hall effect in a frustrated triangular-lattice magnet, Science **365**, 914 (2019).

[45] R. Kumar, S. R. Saha, J. Horn, A. Ikeda, D. Sokratov, Y. Anand, P. Saraf, R. Dorman, E. Hemley, K. K. Iyer, and J. Paglione, Complex single-site magnetism and magnetotransport in single-crystalline Gd_2AlSi_3, Phys. Rev. B **111**, 214426 (2025).

[46] A. P. Ramirez, Strongly geometrically frustrated magnets, Annu. Rev. Mater. Sci. **24**, 453 (1994).